



A study on thermal degradation of zinc oxide nanopowders functionalized with anthocyanins, in correlation with their properties and applications

Anca Dumbrava¹ · Daniela Berger² · Gabriel Prodan³ · Mihaela Badea⁴ · Rodica Olar⁴ · Florin Moscalu⁵ · Aurel Diacon⁶

Received: 29 August 2018 / Accepted: 1 November 2018 / Published online: 14 November 2018
© Springer-Verlag GmbH Germany, part of Springer Nature 2018

Abstract

The variation of structural and optical properties during the thermal degradation of ZnO nanoparticles functionalized with anthocyanins was evidenced through thermal analysis, X-ray diffraction, transmission electron microscopy, electron diffraction, UV–Vis and photoluminescence spectroscopy. A detailed structural study of the particles (cell parameters, lattice strain, and crystallite size) was performed based on the electron diffraction data. The structure and properties were correlated with photocatalytic activity in the degradation of Congo red dye. A higher calcination temperature was associated with lower photocatalytic activity, due to a higher crystallinity. Unusual photoluminescence properties compared to pristine ZnO have been observed.

1 Introduction

Zinc oxide (ZnO) nanoparticles are of much attention for scientists due to their applications based on interesting optical, catalytic, and antimicrobial properties. There are many techniques available for the synthesis of ZnO nanoparticles (chemical precipitation, sol–gel, hydrothermal methods,

chemical vapor deposition, thermal decomposition, electrochemical deposition, laser ablation, combustion method, etc.) and the dependence between synthesis route and properties was highlighted by many studies [1, 2]. Zinc oxide nanopowders obtained in a vegetal matrix by biotechnologies were intensively studied in the recent years [1, 3, 4]. Biosynthesis of nanoparticles means that their preparation was done using microorganisms or plant extracts [3]. The nanoparticles obtained by these methods are capped/functionalized with macromolecules, most often with polysaccharides, but also with vegetal pigments. In green syntheses, the biomolecules act as a matrix, influencing the nanoparticles' morphology [5]. After the nanoparticles' formation, the biomolecules can be removed, by obtaining the pristine ZnO nanoparticles. Despite the several superior properties of capped/functionalized nanoparticles, in some applications highly crystalline pristine nanoparticles are desirable. Withal, the sensitization of semiconductors with pigments, before their application on the conductive glass, can be a convenient procedure for dye sensitized solar cells (DSSCs), but the further annealing of semiconductor layer can destroy the organic pigment. So, in a technology which avoids the annealing of semiconductor layer, the already colored semiconductor powders can be very useful [6], but the annealing of ZnO influences the performance of ZnO-based DSSCs [7, 8]. Considering at least this application, the study of characteristics of the blue ZnO powder annealed at a temperature

✉ Anca Dumbrava
adumbrava@univ-ovidius.ro

¹ Department of Chemistry and Chemical Engineering, Ovidius University of Constanta, 124 Mamaia Blvd., 900527 Constanța, Romania

² Department of Inorganic Chemistry, Physical Chemistry and Electrochemistry, University Politehnica of Bucharest, 1-7 Polizu Str., 011061 Bucharest, Romania

³ Electron Microscopy Laboratory, Ovidius University of Constanta, 124 Mamaia Blvd., 900527 Constanța, Romania

⁴ Department of Inorganic Chemistry, Faculty of Chemistry, University of Bucharest, 90-92 Panduri Str., 050663 Bucharest, Romania

⁵ Department of Physics, Ovidius University of Constanta, 124 Mamaia Blvd., 900527 Constanța, Romania

⁶ Department of Bioresources and Polymer Science, University Politehnica of Bucharest, 1-7 Polizu Str., 011061 Bucharest, Romania

of 450 °C or higher is interesting. The removal of organic template led to pristine ZnO, whose structure and properties were influenced by the removed template, so it is motivating to study the resulting powder.

As a synthesis method, the thermal treatment has the advantage of obtaining high purity materials. High purity and crystallinity of zinc oxide are important for applications like ZnO-based electronic devices (electrical insulations and varistor ceramics [9], metal insulator semiconductor, ultraviolet photodetectors [10], laser diodes, light-emitting diodes, piezoelectric transducers and generators, gas sensors [11], etc.). Several thermal treatments were used to synthesize ZnO nanoparticles, with various shapes [12–14]. The studies demonstrated that, beside the synthesis temperature, the post-synthesis heat treatment of ZnO nanoparticles also influences its properties [15]. Although the thermal treatment is efficient in synthesis of pure ZnO, its disadvantage is the accompanying undesirable nanoparticle sintering, which leads to larger particles/grains [9].

We studied the effect of thermal treatment on the structure and properties of anthocyanins functionalized ZnO nanoparticles. The result of calcination at three different temperatures on the structure and morphology of ZnO nanopowders was investigated in detail by transmission electron microscopy and electron diffraction, and confirmed by X-ray diffraction. In addition to the morphology, the particle size and the lattice strain were determined using Scherrer's equation and Williamson–Hall method applied for electron diffraction data [16–18]. The novelty of our study consists in the nature of starting material. The influence of ZnO nanopowders synthesis route on their thermal behavior and calcination products' properties is highlighted in comparison with pristine ZnO nanopowders obtained through different methods [19–21]. The TEM study of thermal decomposition aims to contribute to the improvement of information regarding the thermal behavior of functionalized ZnO nanopowders. The effect of thermal treatment on the photocatalytic activity of ZnO for wastewater treatment is also considered.

2 Experimental

2.1 Materials

The high purity reagents were obtained from Sigma-Aldrich (zinc acetate, $\text{Zn}(\text{CH}_3\text{COO})_2 \cdot 2\text{H}_2\text{O}$; Congo red), Merck (hydrochloric acid, HCl, 37%) and Loba Chemie (sodium hydroxide, NaOH), being used as received without further purification. The Congo red (CR, C.I. Direct Red 28, M.W. = 696.67 g mol⁻¹, $\text{C}_{32}\text{H}_{24}\text{N}_6\text{O}_6\text{S}_2\text{Na}_2$) is the disodium salt of 3, 3'-([1,1'-biphenyl]-4,4'-diyl)bis(4-aminonaphthalene-1-sulfonic acid). Red cabbage (*Brassica oleraceae*) was purchased from Romanian local market.

2.2 Synthesis of ZnO nanopowders

The zinc oxide nanopowders functionalized with anthocyanins (ZnO@antho **1** and ZnO@antho **2**) were prepared as in our previous article [18]. In brief, ZnO@antho **1** nanopowder was obtained by chemical precipitation in a red cabbage aqueous extract (5 g sliced fresh leaves in 50 mL distilled water acidulated with 1 mL of 1M HCl solution), using $\text{Zn}(\text{CH}_3\text{COO})_2 \cdot 2\text{H}_2\text{O}$ as precursor and a solution of NaOH 1 M (one-pot synthesis). ZnO@antho **2** nanopowder was obtained by sensitization of a pristine ZnO nanopowder (obtained in an aqueous solution by chemical precipitation, from same reagents as above) with anthocyanins from a red cabbage aqueous extract. The calcination of ZnO@antho **1** nanopowder was performed in a laboratory furnace (Labertherm L 9/11/B170), with a heating rate of 10 °C/min. The calcinated samples were obtained by heating ZnO@antho **1** nanopowder for 2 h at 450 °C (ZnO-450), 600 °C (ZnO-600), and 800 °C (ZnO-800), respectively.

2.3 Characterization of ZnO nanopowders

The powders were investigated by X-ray diffraction (XRD) performed on a Rigaku Miniflex 2 diffractometer with Ni filtered $\text{CuK}\alpha$ radiation, in the range of 2θ , 10–70°, scan rate of 2°/min and a step of 0.02°. The transmission electron microscopy (TEM), high-resolution transmission electron microscopy (HRTEM) and selected area electron diffraction (SAED) were performed on a Philips CM 120 ST transmission electron microscope operated at 100 kV, with 2 Å resolution. The electron diffraction (ED) structure analysis was based on data obtained from electron diffraction patterns, for a chamber length of 880 nm and an acceleration voltage of 100 kV, conditions for which the calculation constant of interplanar distance is $446.5 \text{ mm } \text{Å} \left(d_{hkl}(\text{Å}) = \frac{446.5 (\text{mmÅ})}{D(\text{mm})} \right)$.

The analysis of electron diffraction patterns was achieved with CRISP2 application, in the polycrystalline materials mode (ELD). The indexation of lines extracted from profile was done by comparison method. The UV–visible diffuse reflectance spectra of ZnO powders were recorded in the range of 220–850 nm, on a Jasco V-550 spectrophotometer with an integrating sphere, using MgO as the reference. The photoluminescence (PL) spectra were recorded on a Jasco FP-6500 spectrofluorometer. The thermogravimetric (TG) and differential thermal analysis (DTA) curves were recorded using a Labsys 1200 SETARAM instrument, over the temperature range of 30–900 °C and a heating rate of 10 °C min⁻¹. The measurements were carried out in synthetic air atmosphere (flow rate 16.66 cm³ min⁻¹), using alumina crucibles.

2.4 Catalytic properties of zinc oxide nanopowders

The procedure for photocatalytic experiments was described in our previous studies [18, 22, 23]. The CR degradation was monitored by UV–Vis spectroscopy, in the range of 200–900 nm, on a Jasco V-550 spectrophotometer. The maximum of absorption for initial CR solution was identified at 498 nm. The photodegradation of CR was estimated by C_t/C_0 ratio (where C_t and C_0 are the concentrations of CR at certain time, t , and initial concentration, respectively). The efficiency of ZnO nanopowders as a photocatalyst was evaluated by the photocatalytic activity (PA):

$$PA = \frac{C_0 - C_t}{C_0} \times 100 = \frac{A_0 - A_t}{A_0} \times 100, \quad (1)$$

where A_0, A_t are the absorbance value for CR solutions when the reaction time is 0 and t , respectively (based on Lambert–Beer law) [24].

3 Results and discussion

3.1 Thermal degradation

We studied the thermal decomposition in air of anthocyanins functionalized ZnO nanopowder, obtained by one-pot method (ZnO@antho 1), which was performed in comparison with ZnO nanopowder colored with anthocyanins (ZnO@antho 2).

Table 1 shows the thermal decomposition data in air for the ZnO samples. The ZnO@antho 1 nanopowder decomposes in four steps (Fig. 1a). First, physisorbed water molecules are released at a low temperature (60–136 °C) indicating the hydration of zinc oxide powder [25]. The next three exothermic steps, which occur in the 136–475 °C temperature range, correspond to organic moieties decomposition with an overall mass loss of 10.7%. Having in view the weak exothermic effect of the second event, we can assume that several processes such as bonds cleavage and oxidative degradation of some fragments occur

Table 1 Thermal decomposition data in air for ZnO@antho samples

Compound	Step	Thermal effect	Temperature (°C)	Δm_{exp} (%)
ZnO@antho 1	1	Endothermic	60–136	2.3
	2	Exothermic	136–257	4.6
	3	Exothermic	257–375	4.7
	4	Exothermic	375–475	1.4
	Residue (ZnO)			87
ZnO@antho 2	1	Endothermic	60–110	1.6
	2	Exothermic	110–239	7.4
	3	Exothermic	239–292	1.2
	4	Exothermic	292–490	2.4
	Residue (ZnO)			87.4

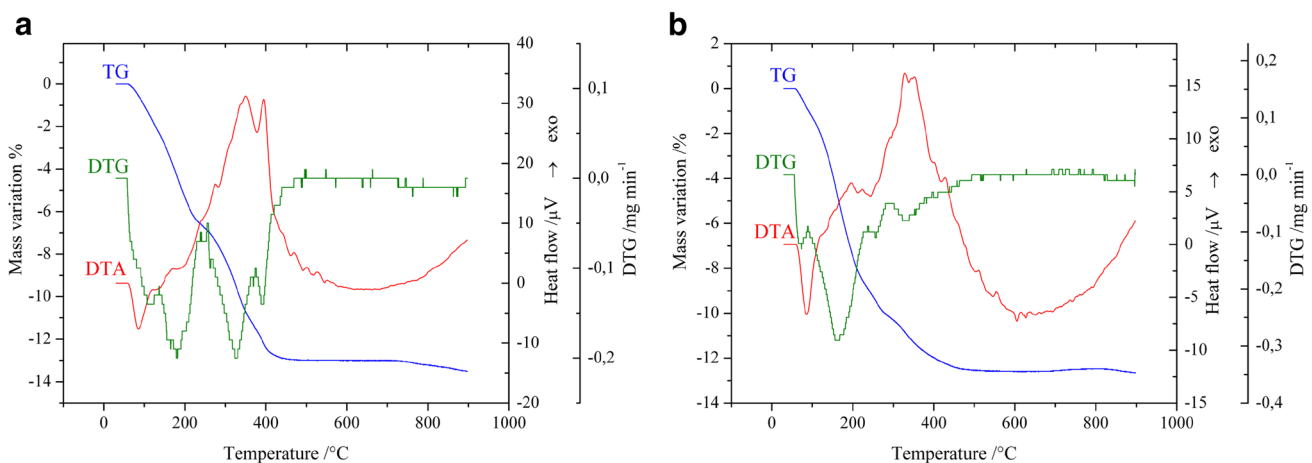


Fig. 1 TG, DTG and DTA curves for ZnO@antho 1 (a) and ZnO@antho 2 (b)

simultaneously. The strong exothermic effects that accompany the last two steps can be assigned to the aerobic combustion of organic residue [25].

ZnO@antho **2** sample decomposes also in four steps, as can be seen in Fig. 1b. The water molecules are eliminated at a lower temperature (60–110 °C) comparatively with the previously discussed compound, suggesting that hydration water is involved in less hydrogen bonding [25]. The organic part, that represents 11% (wt), is eliminated also in three exothermic steps (110–490 °C). Unlike the Zn@antho **1**, this species lost the most part of organic moieties (7.4%) up to 240 °C indicating that these are weakly retained in the compound network [25]. The residual organic mass undergoes oxidative degradation up to 490 °C. For both species the final residue is zinc oxide as XRD powder indicates.

The thermal decomposition also demonstrated the differences between the synthesis methods for blue ZnO@antho nanopowders. The stronger bonding of pigment molecules in the case of ZnO@antho **1** sample obtained by one-pot method was confirmed.

3.2 TEM study of ZnO nanopowders

The powders obtained by thermal decomposition of Zn@antho **1** sample were the subject of a TEM study. Because electrons interact much more strongly with matter than X-rays, both HRTEM images and ED patterns can be obtained from nanosized crystals [26].

The morphology of particles was revealed by bright-field TEM (BFTEM) images (Fig. 2). As shown in Fig. 2b–d, the particles of all samples have an almost spherical shape, with a factor shape of 0.84 (ZnO-450), 0.81 (ZnO-600), and 0.86 (ZnO-800), calculated from measured diameters. It is obvious that the flake-like shape of anthocyanins functionalized ZnO particles (Fig. 2a) changed during the thermal treatment.

The values of Feret diameter (d_F) were evaluated from TEM images using a semi-automated algorithm implemented in the analysis software [27]. Figure 3 shows histograms of the particle size distributions together with the Gaussian profiles, demonstrating the increase of Feret diameter with calcination temperature from 27.34 nm

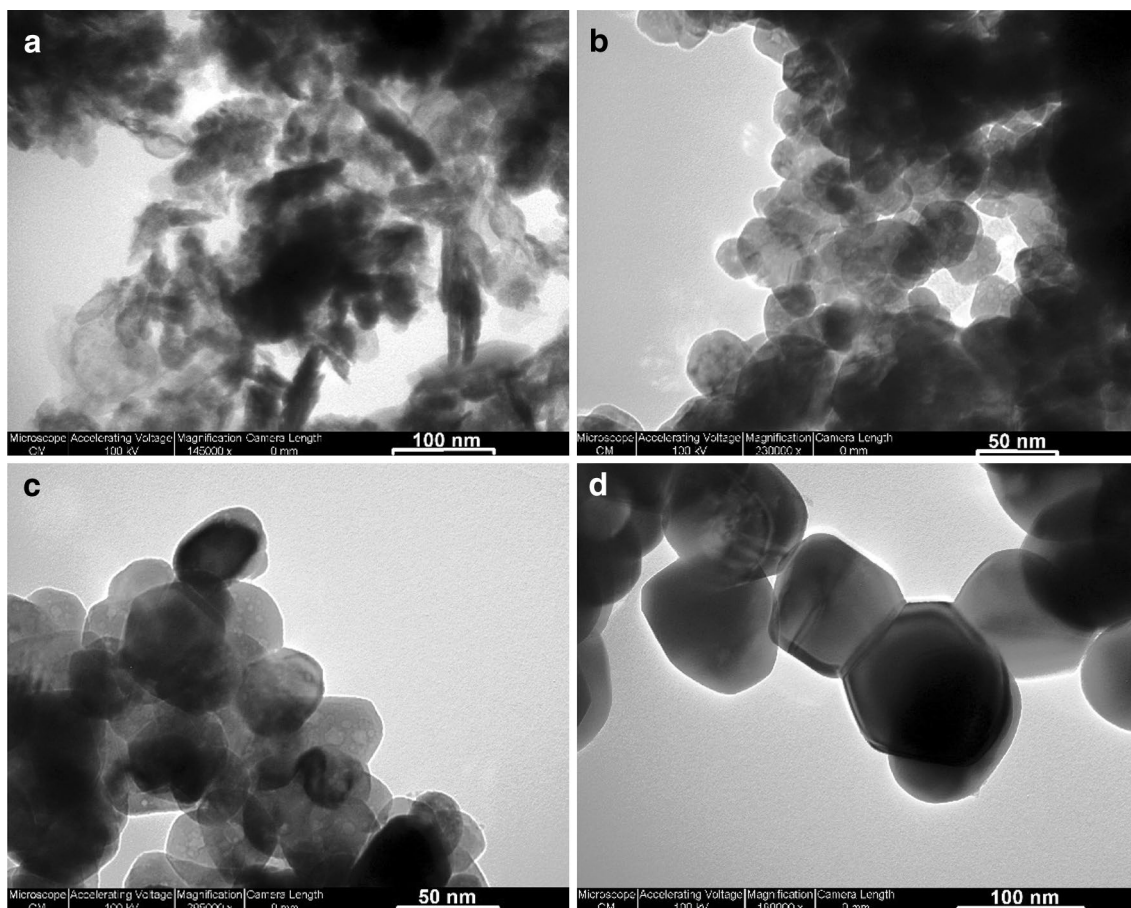


Fig. 2 The BFTEM images of ZnO@antho **1** before (a) and after calcination at 450 °C (ZnO-450) (b), 600 °C (ZnO-600) (c), and 800 °C (ZnO-800) (d)

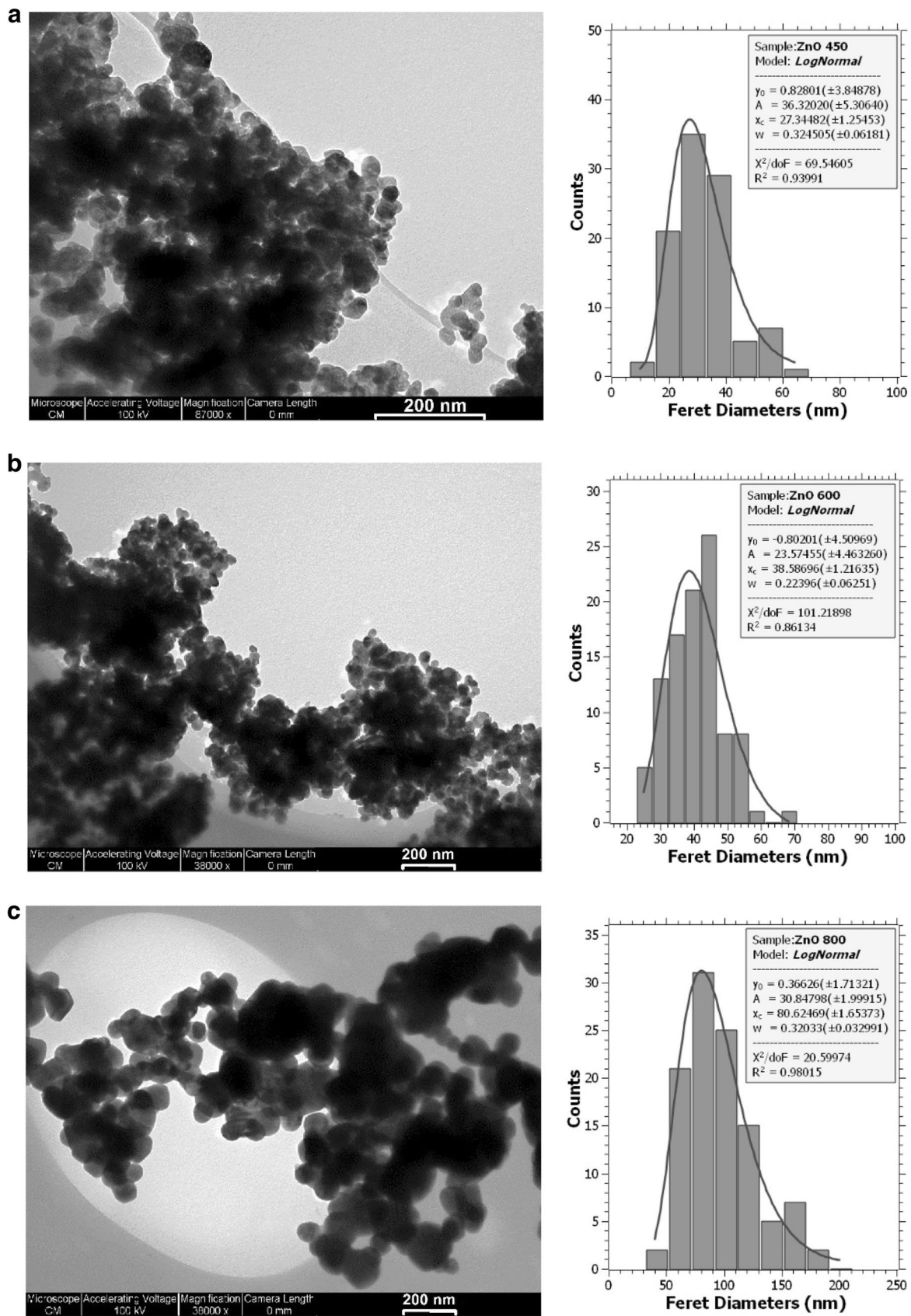


Fig. 3 The area selected for TEM morphological analysis and the particle diameters distribution for ZnO-450 (a), ZnO-600 (b), and ZnO-800 (c)

(ZnO-450) to 48.57 nm (ZnO-600) and 80.62 nm (ZnO-800), superior to value for starting material ($d_F = 23.16$ nm [18]). The results demonstrated the increase of aggregates during the thermal treatment, as it was also noticed by other authors [9, 28].

The ED patterns were used for the identification of particles structure. The profiles extracted from the electron diffraction patterns (Fig. 4) demonstrated the hexagonal wurtzite structure of crystallites [29], which is in good agreement with XRD data.

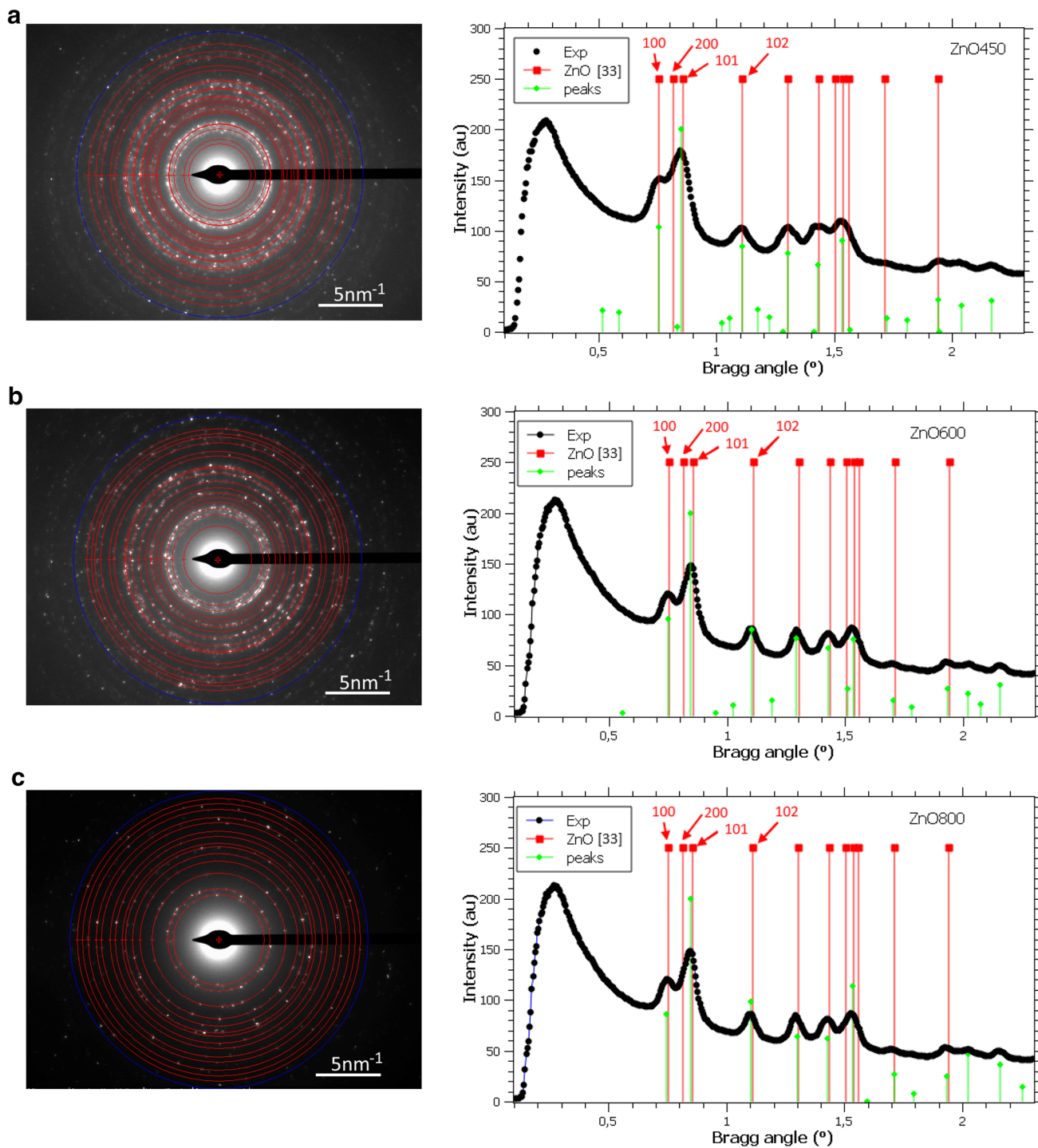


Fig. 4 **a** SAED pattern (left) and ED profile (right) for ZnO-450 nanopowder. **b** SAED pattern (left) and ED profile (right) for ZnO-600 nanopowder. **c** The SAED pattern (left) and ED profile (right) for ZnO-800 nanopowder

A central topic in nanoscience is the accurate measurement of particle sizes. This objective became even more important with the discovery of the quantum size effect. Together with XRD technique, the electron microscopy is one of the most commonly used techniques developed to determine the diameter of nanoparticles [30]. The crystallite size was determined from ED (Fig. 4a–c) using the Scherrer equation [31] and the values are listed in Table 2. The results demonstrated that a nanopowder consisting of crystallites with mean size of 5.00 nm was obtained by calcination of anthocyanins functionalized ZnO nanopowder at 450 °C. By increasing the calcination temperature, the crystallites' dimension also increased (6.23 nm for ZnO-600 and 8.10 nm for ZnO-800). The same trend was identified for Feret diameter, as it was described above.

The lattice constants (Table 2) were determined by Cohen method of least squares [32], based on electron diffraction data (Fig. 4a-c). The obtained values are similar to those reported for zincite (Institute of Experimental Mineralogy Data Base, Card No. 5364) [33].

The Williamson–Hall analysis, an integral breadth method, was used for the determination of strain effect in ZnO lattice [34]. The lattice strain, a measure of the distribution of lattice constants, arises from crystal imperfections (e.g., lattice dislocation), and also from grain boundary triple junction, contract or sinter stresses, stacking faults, coherency stresses, etc. [16, 31]. A negative strain for calcined ZnO particles was also noticed by other authors [16]. The strain can be determined by the lattice shrinkage, which was also observed in the calculation of some lattice parameters.

A previous study demonstrated that the thermal treatment of the polycrystalline zinc oxide at higher temperatures than 750 °C results in the formation of long-life thermal defects [35], which can explain the increase of lattice strain (absolute value) for ZnO-800 in comparison with ZnO-600 sample.

Very small errors can be found in Table 2 for values calculated by Cohen method. The Williamson–Hall curves and the values for relative strain of lattices confirmed the errors.

3.3 XRD

The crystal structure and phase composition of ZnO samples were also determined by XRD, as a complementary technique for ED. Many studies are dedicated to the comparison of different methods for investigation, demonstrating that XRD and ED have both advantages and disadvantages in determination of structure and crystals' dimension [30].

XRD patterns (Fig. 5) confirm that ZnO samples have hexagonal wurtzite structure ($P6_3mc$ space group in the Hermann–Mauguin notation, JCPDS 36-1451) [29, 36]. No characteristic peaks of any impurities or secondary phase were detected.

The crystallite size for ZnO powders has been determined with Rigaku PDXL software, from XRD data, based on Scherrer's equation from (1 0 1) diffraction peak. The calcination of anthocyanins functionalized ZnO nanopowder at 450 °C results in increase of crystallite size from 17.7 nm (ZnO@antho 1 [18]) to 22.7 nm (for ZnO-450). A small size increase was noticed by the rise of calcining temperature from 450 to 600 °C (25.1 nm for ZnO-600),

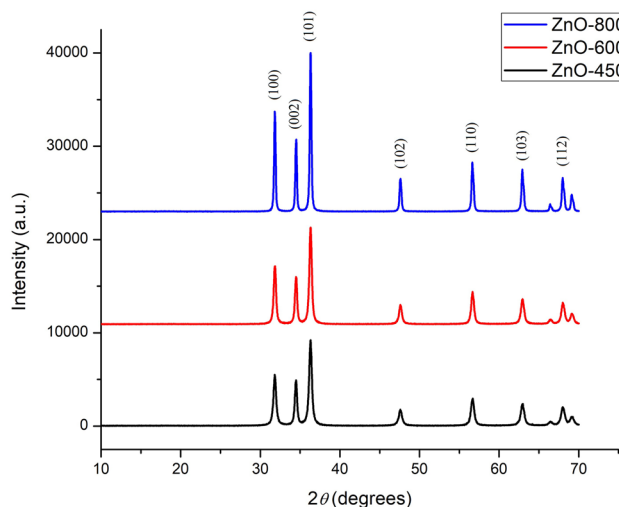


Fig. 5 XRD patterns of ZnO nanopowders

Table 2 The crystallite size (Scherrer equation), cell parameters ($P6_3mc$ space group, $a = b = 3.2494 \text{ \AA}$ and $c = 5.2038 \text{ \AA}$ for zincite-5364 [33]) and relative strain of lattice, calculated from electron diffraction patterns

Sample	Crystallite size (nm)	Cell parameters			Relative strain of lattice (ϵ)
		Derived from the specified (h k l) line	Cohen method	Errors (%)	
ZnO-450	5.00	(1 0 0) $a = 3.2346 \text{ \AA}$	$a = 3.2457 \text{ \AA}$	-0.10212	-0.00617
		(0 0 2) $c = 5.4885 \text{ \AA}$	$c = 5.2076 \text{ \AA}$	0.01297	
ZnO-600	6.23	(1 0 0) $a = 3.2572 \text{ \AA}$	$a = 3.2768 \text{ \AA}$	0.85704	-0.00517
		(1 0 2) $c = 5.2553 \text{ \AA}$	$c = 5.2593 \text{ \AA}$	1.00557	
ZnO-800	8.10	(1 0 0) $a = 3.2347 \text{ \AA}$	$a = 3.2497 \text{ \AA}$	-0.10212	-0.00589
		(0 0 2) $c = 5.0950 \text{ \AA}$	$c = 5.2076 \text{ \AA}$	0.01297	
		(1 0 1) $c = 5.4885 \text{ \AA}$			

but a greater increase in the case of the thermal treatment at 800 °C (42.4 nm for ZnO-800).

3.4 Optical properties of ZnO nanopowders

The optical properties of ZnO nanoparticles were studied by UV–visible diffuse reflectance spectroscopy and photoluminescence spectroscopy. The UV–Vis spectra of ZnO nanopowders obtained by thermal degradation are presented in Fig. 6. The maximum of absorption band is situated in UV domain, at values which increase with calcination temperature. The position of absorption band for ZnO samples can be correlated with the particles dimension, a red shift for larger particles obtained at higher temperatures being evidenced.

The UV–Vis spectrum of ZnO-800 sample has a slightly different shape in comparison with ZnO-450 and ZnO-600, with a sharper absorption peak at 368 nm. Mikhailov et al. [35] demonstrated that over 750 °C the processes which occur in ZnO powder modify the electron distribution. The free electron concentration decreases during the thermal

the surface, the thermal ionization of lattice zinc atoms and ions, and the capture of free electrons by anion vacancies. The coloring centers can also be formed at the defects of the cation sublattice induced by desorption of the chemisorbed groups, such as OH⁻ [35].

The band gap energy and Brus diameter were calculated from UV–Vis spectra. We estimated the band gap energy (E_g) using Tauc equation (Fig. 7). The point of extrapolation on the abscissa of Tauc plot ($(\alpha h\nu)^2$ versus $h\nu$) linear part gives the band gap energy value for the material [37]. A decrease of the band gap energy with the particle size increase can be noticed. The particle size influences the semiconductor properties, and the relationship between band gap and particle dimension was demonstrated by several studies [38].

The particle size for ZnO samples was determined from the band gap values, in the effective mass approximation (EMA), using the Brus formula [38, 39]. In the approximation of a spherical shape, justified by the shape factor values, we calculated the particle diameter from the blue shift of the band gap values:

$$E_g - E_{g,0} = \frac{\hbar^2 \pi^2}{2m_0 r^2} \left(\frac{1}{m_e^*} + \frac{1}{m_h^*} \right) - \frac{1.8 e^2}{4\pi \epsilon_0 \epsilon_r r} - \frac{0.124 e^4 m_0}{\hbar^2 (4\pi \epsilon_0 \epsilon_r)^2} \left(\frac{1}{m_e^*} + \frac{1}{m_h^*} \right)^{-1}, \quad (2)$$

treatment because of the electrons capture, by the thermal desorption anion vacancies on the surface and also by unsaturated lattice atoms on the powder surface. The possible color of powder is explained by the formation of electron coloring centers, due to several processes which occur simultaneously, like the thermal desorption of gases from

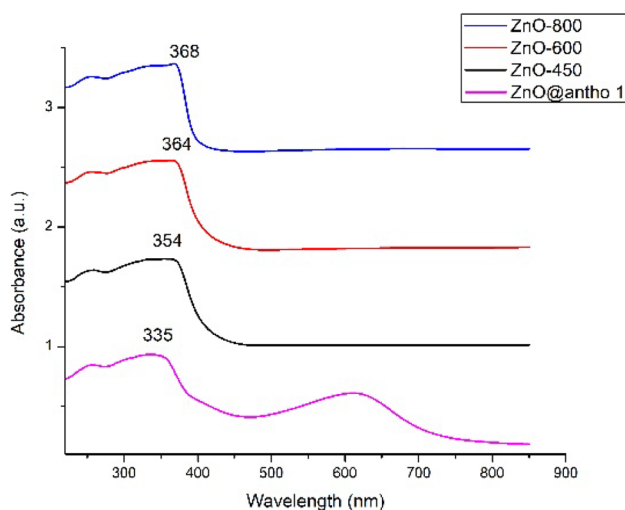


Fig. 6 UV–Vis absorption spectra for calcined ZnO nanopowders, in comparison with anthocyanins functionalized ZnO [18]

where E_g = band gap value determined from the absorption spectrum via Tauc plot; $E_{g,0} = 3.30$ eV (band gap value for ZnO wurtzite [40]); $m_e^* = 0.24$ (relative effective mass of electron [41]); $m_h^* = 0.59$ (relative effective mass of hole [41]); m_0 = electron mass; ϵ_0 = dielectric constant of vacuum; $\epsilon_r = 8.66$ (relative dielectric constant [42]) and r = particle radius.

A good agreement between the values calculated for particles diameter using the Brus formula (Table 3) and those

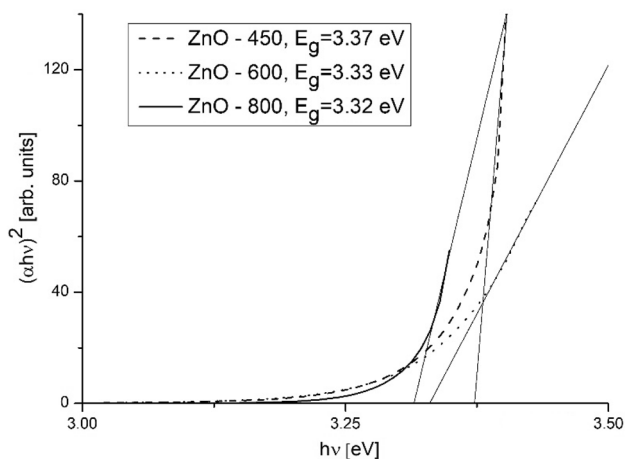


Fig. 7 Tauc plots for ZnO samples

Table 3 The particles diameter calculated with Brus formula, in correlation with band gap energy values

Sample	E_g (eV)	Particle diameter (Brus) (nm)
ZnO-450	3.37	7.74
ZnO-600	3.33	9.86
ZnO-800	3.32	10.82

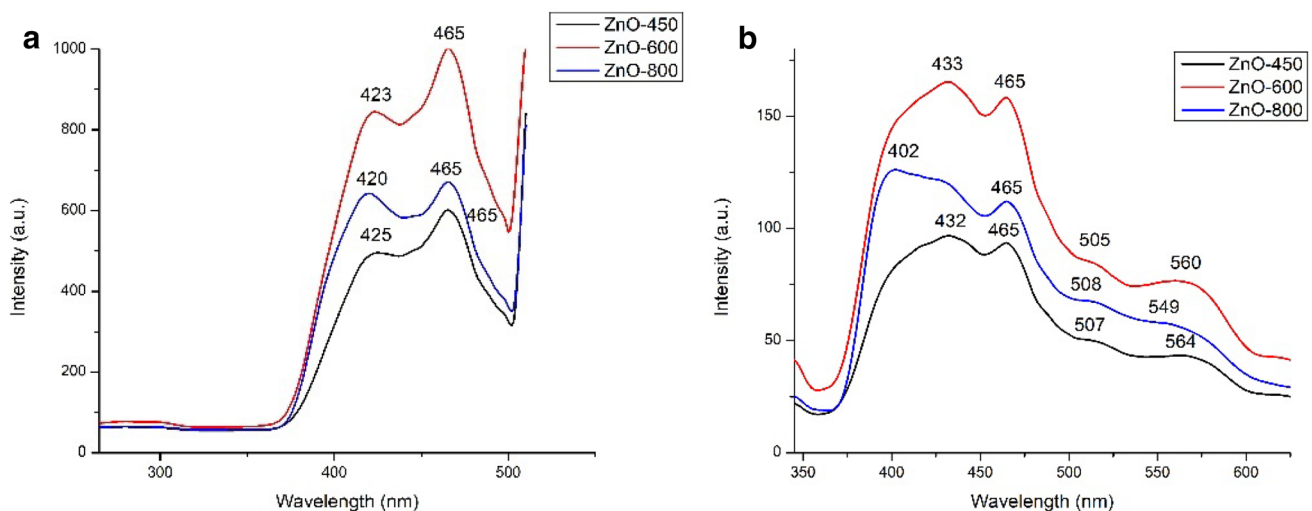
obtained from electron diffraction data (Table 2) can be evidenced. The correlation between band gap energy and Brus diameter, meaning the stronger confinement (the smallest nanoparticle diameter) the greater value for band gap, can be noticed.

Photoluminescence spectroscopy is a proper method for investigating the electronic structure of materials. The excitation with two different wavelength radiations (260 and 340 nm, respectively) was used for PL spectra of ZnO nanopowders. For PL spectra of semiconductors there are characteristic two emissions bands, i.e., a sharp band, near the absorption edge (“excitonic photoluminescence”, associated with band-to-band excitonic recombination) and a broad band, at longer wavelength (“trapped photoluminescence”, originated by deep-level emissions) [43, 44]. The UV-emission band is due to the recombination of an electron at the zinc interstitial and a hole in the valence band. The visible emission band corresponds to the electron transition from the conduction band to interstitial oxygen defects in zinc oxide [19]. The PL spectra for ZnO are dominated by strong near band edge emission originating from free exciton emission and the intensity of first peak can be related to the crystallinity quality of the ZnO particles [44].

As can be seen in Fig. 8, for all three ZnO samples, using both excitations of 260 and 340 nm, the first strong emission band is broad (370–500 nm) and splitted into two partially overlapped bands. The position of first peak for ultraviolet emission band (Fig. 8a) approximates the band gap of ZnO [11]. The broad shape of the peaks indicates that a large amount and, probably, a variety of donor species is incorporated into the powders [44], generated by the thermal decomposition of capping organic compounds.

Two other emission bands in PL spectra of ZnO samples are observed in the visible domain, ranging from 500 to 600 nm (Fig. 8b). The emission is caused by the recombination of photogenerated charges with various kinds of intrinsic crystal defects (like neutral or charged O/Zn vacancies, interstitials, and anti-sites) [11, 45]. The increase of intensity for emission bands from ZnO-450 to ZnO-600 can be associated with the decrease of photocatalytic activity.

The intensity ratio between the near band edge UV emission and the visible region is usually used to evaluate the quality of ZnO [19]. As it was reported, the calcination of pristine ZnO in the temperature range of 200–500 °C revealed that the ultraviolet emission peak of the samples calcined at higher temperature become more intense, sharper, and narrower, while the visible emission peak become less intense compared to UV emission [19]. In our study, in the considered temperature range, a different feature was identified. The influence of initial ZnO structure, composition and properties on the distribution of electrons in energy bands, and on the defects concentration can be noted by comparison of the PL spectra with those obtained for ZnO powders synthesized by calcination of pristine ZnO [19, 45]. The particle shapes and the presence of impurities also influence the photoluminescence properties [46].

**Fig. 8** PL spectra of ZnO samples, using an excitation wavelength of 260 nm (a), respective 340 nm (b)

3.5 Photocatalytic properties

The photocatalytic activity of calcined ZnO nanopowders functionalized with anthocyanins was determined in the degradation of Congo red in aqueous solutions. We measured the absorbance at 498 nm (the azo bond degradation) as a function of irradiation time. The photocatalytic activity of ZnO nanopowders was estimated by the C_t/C_0 ratio (Fig. 9a) for a rate of 0.05 g catalyst/100 mL CR solution of 30 mg/L.

By calcination of ZnO@antho **1** at 450 °C, lower value for photocatalytic activity in comparison with that of functionalized ZnO nanopowder [18] was determined. The catalytic activity of ZnO decreased with the increase of crystallinity, so the lowest photocatalytic activity was assigned to ZnO-800, for which the largest crystallite size was calculated. For example, after 90 min the highest PA value was obtained for ZnO-450 (80.48%), followed by ZnO-600 (74.41%) and ZnO-800 (57.60%), whereas 86.44% was obtained for blue ZnO@antho **1** [18]. In the absence of catalyst, an insignificant variation of CR concentration was identified [23], demonstrating the high stability of the dye.

The lattice strain can be correlated with the crystal defects and accordingly with photocatalytic activity, because the defects (i.e., intrinsic and foreign, bulk and surface defects) play an important role in the photocatalysis through their concentration and distribution [47]. The highest absolute value for lattice strain was calculated for ZnO-450 ($|\epsilon| = 0.00617$), with lower crystallinity and highest photocatalytic activity.

By comparing the structure and properties of ZnO-450 with ZnO-600 powder, an increase of crystallite size, and

also of aggregate size, involves a lower surface area and thus a decrease of photocatalytic activity from ZnO-450 to ZnO-600. This observation is also in agreement with higher intensity of emission bands in PL spectrum of ZnO-600 powder (the lower photoluminescence emission intensity, the lower recombination rate of the photogenerated electron–hole pairs, the higher photoactivity).

For the lowest photocatalytic activity of ZnO-800 powder, the explanation involves the increase of crystallites and aggregates' size. Despite a lower intensity of emission bands in PL spectrum, compared to ZnO-600, the dominant factor seems to be the particles' dimension. A similar behavior was reported for TiO₂ powder, i.e., a decrease of photocatalytic activity by calcination above 400 °C due to the decreased surface area, because of the reduced boundaries between the subunits and surface roughness of the nanoparticles [48].

ZnO nanopowders obtained by a variety of synthesis routes have been tested as photocatalysts for the degradation of several azo dyes. An accurate comparison with other photocatalytic systems involves the consideration of factors which influence the photocatalysis, especially the dye/catalyst ratio and time of reaction. In similar conditions, the nanopowders of pristine ZnO obtained by calcination have a good photocatalytic activity, but inferior to that of less crystalline ZnO nanopowder obtained by chemical precipitation in aqueous solution or in vegetal extract (Table 4).

The kinetic parameters were calculated for a quantitative evaluation of photocatalytic process (Table 5). The decomposition of an organic dye on a semiconductor is a heterogeneous catalysis in which are involved processes as carrier generation, carrier transport, carrier recombination (on the surface and in bulk), carrier interfacial

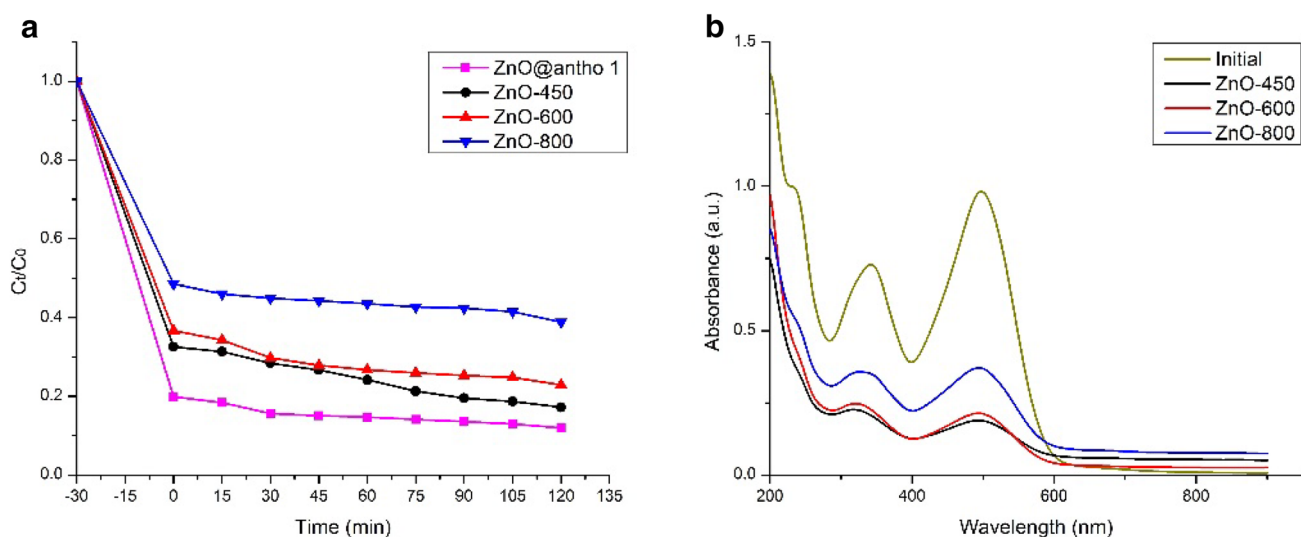


Fig. 9 **a** The photocatalytic degradation curves of CR over the calcined ZnO nanopowders, in comparison with ZnO nanopowder functionalized with anthocyanins [18]. **b** UV-Vis spectral changes of CR solutions after the photocatalytic process

Table 4 Comparison between photocatalytic activity of ZnO powders in the degradation of organic dyes

Photocatalyst	Azo dye	Amount of photocatalyst (mg)	Amount of azo dye (mg)	Time (min)	PA%	References
ZnO nanoparticles (hydrothermal synthesis)	Rhodamine B	100	0.5	120	67%, 94%, 48% and 73%	[49]
ZnO nanotetrapods	Rhodamine B	20	0.16	60	92%	[50]
Commercial bare ZnO nanoparticles	Methylene blue	10	0.128	30	40%	[51]
Protein-capped ZnO nanoparticles	Methylene blue	10	0.128	30	90%	[51]
Pristine ZnO nanopowder (chemical precipitation)	Congo red	50	3	60	79.20	[18]
ZnO nanopowder sensitized with anthocyanins (ZnO@antho 2)	Congo red	50	3	60	58.75	[18]
ZnO nanopowder functionalized with anthocyanins (ZnO@antho 1)	CR	50	3	60	85.28	[18]
ZnO-450	CR	50	3	60	75.80	This work
ZnO-600	CR	50	3	60	73.3	This work
ZnO-800	CR	50	3	60	56.42	This work

Table 5 Kinetic parameters (reaction rate, k_{app} ; experimental and calculated value of initial concentration, Q_0 ; regression coefficient, R) for the photocatalytic degradation of CR dye with ZnO nanopowder catalysts (0–120 min)

Sample	$Q_{0, experimental}$ (mg/L)	L–H simplified model		
		Q_0 (mg/L)	k_{app} (min^{-1})	R^2
ZnO-450	7.80	8.02	0.0056	0.990
ZnO-600	8.79	8.31	0.0036	0.922
ZnO-800	11.19	11.15	0.0016	0.921

transfer, and subsequent organic oxidations [47]. All these processes must be considered in a kinetic model, and Langmuir–Hinshelwood (L–H) model, a widely accepted kinetic mechanism, covers as well the adsorption properties of the substrate on the photocatalyst surface. Assuming that the reactant is strongly adsorbed on the catalyst surface than the products, the rate of unimolecular surface reaction in L–H model is proportional to the surface coverage [52]. The kinetic of the photocatalytic process fits the L–H simplified equation [53] which can be written in a linearized form:

$$\ln Q = \ln Q_0 - k_{app} \times t, \quad (3)$$

where Q is the concentration of the reactant (mg/L), Q_0 is the initial value of Q and t is the illumination time. Performing a linear fit of the plot of $\ln Q$ against time, the slope and the intercept of trend line give the values of k_{app} and Q_0 , respectively. The L–H kinetic type for photocatalytic degradation is supported by very close to unit values of R^2 and small difference between Q_0 and $Q_{0,exp}$ (Table 5). The experimental values of concentration after the adsorption

in dark (Q_0) are inversely proportional with the adsorption capacity of ZnO nanopowder, increasing from ZnO-450 to ZnO-800, as the reaction rate decreases. The ZnO-450 nanopowder is characterized by both highest adsorption capacity and photocatalytic reaction rate, which decrease to ZnO-600 and then to ZnO-800.

The UV–Vis spectra of CR solutions over ZnO catalysts demonstrated not only the breakdown of the azo bond (the chromophore), but also the decomposition of CR in smaller species, because the intensity of band assigned to aromatic rings in the electronic spectra also decreases in time (Fig. 9b). This is an important feature in the treatment of the wastewaters from textile industry, because the simple breakdown of the azo bonds is not enough for the environmental safety, since the toxic products can remain in water. The mineralization of CR can be also demonstrated by the decrease of pH value, proving the obtaining of oxidation products which increase the acidity of solution (e.g., CO_2) [54]. The pH of CR solution varied from 8.20 for the initial solution to 7.60 (ZnO-450), 7.65 (ZnO-600) and 7.70 (ZnO-800), a lower final value of the solution pH being correlated with a higher photocatalytic activity of ZnO powder tested as catalyst.

4 Conclusions

The thermal decomposition of blue ZnO nanopowders obtained in red cabbage extracts, by one-pot synthesis and by sensitization with anthocyanins, was performed in air, demonstrating similar quantities of organic compounds in the composite materials (10.7% and 11%, respectively). A stronger interaction between organic and inorganic

components, revealed by a higher temperature for organic part loosing, was identified in the sample obtained by one-pot synthesis.

Pristine ZnO nanopowders were obtained by calcination of ZnO functionalized with anthocyanins at 450, 600, and 800 °C. The XRD results demonstrated the increase of crystallites' size with calcination temperature, from 22.7 nm (ZnO-450) to 25.1 nm (ZnO-600) and 42.4 nm (ZnO-800). The ED technique confirmed a similar trend in increase in the crystallites' size, from 5.00 nm (ZnO-450) to 6.23 nm (ZnO-600) and 8.10 nm (ZnO-800). The values of Feret diameter for nanoparticles, calculated from TEM images, verified the same increase with temperature (27.34 nm for ZnO-450, 48.57 nm for ZnO-600, and 80.62 nm for ZnO-800). The nanoparticles are almost spherical, with a factor shape of 0.84 (ZnO-450), 0.81 (ZnO-600), and 0.86 (ZnO-800).

The increase of crystallinity caused the modification of optical properties (determined by UV–Vis and PL spectroscopy). Thus, the band gap energy decreased with calcination temperature growth (3.37 eV for ZnO-450, 3.33 eV for ZnO-600, and 3.32 eV for ZnO-800). The unusual PL properties of calcined ZnO samples can be assigned to the species incorporated in nanopowders during the thermal decomposition of organic compounds, the defects' concentration being also influenced by calcination temperature. The decrease of photocatalytic activity in the degradation of Congo red azo dye can be correlated with the thermal treatment temperature too (e.g., after 120 min the fraction of removed CR was 82.79% for ZnO-450, 77.11% for ZnO-600 and 61.15% for ZnO-800).

Our study illustrated the modification of structure and properties of ZnO nanopowders functionalized with anthocyanins, obtained in a vegetal matrix, during thermal treatment. For a proper combination between a good crystallinity, optical properties and still a high surface area, with benefits in photocatalytic applications, a temperature of 450 °C for calcination is suitable.

Acknowledgements This work has been performed in the frame of Project no. 91, JINR-RO 2018, topic number 04-4-1121-2015/2020, JINR 322/21.05.2018, Dubna, Russia.

References

1. S. Ahmed, S.A. Annu, S. Chaudhry, Ikram, J. Photochem. Photobiol. B **166**, 272 (2017). <https://doi.org/10.1016/j.jphotobiol.2016.12.011>
2. H. Morkoç, Ü Özgür, *Zinc Oxide: Fundamentals, Materials and Device Technology* (Wiley-VCH Verlag, Weinheim, 2009)
3. H. Agarwal, S. Venkat Kumar, S. Rajeshkumar, Resour. Effic. Technol. **3**, 406 (2017). <https://doi.org/10.1016/j.refffit.2017.03.002>
4. H. Mirzaei, M. Darroudi, Ceram. Int. **43**, 907 (2017). <https://doi.org/10.1016/j.ceramint.2016.10.051>
5. G. Sangeetha, S. Rajeshwari, R. Venkatesh, Mater. Res. Bull. **46**, 2560 (2011). <https://doi.org/10.1016/j.materresbull.2011.07.046>
6. L. Zhang, A. Konno, Int. J. Electrochem. Sci. **13**, 344 (2018). <https://doi.org/10.0964/2018.01.07>
7. A.M. Golsheikh, K.Z. Kamali, N.M. Huang, A.K. Zak, Powder Technol. **329**, 282 (2017). <https://doi.org/10.1016/j.powtec.2017.11.065>
8. A. Al-Kahlout, J. Assoc. Arab. Univ. Basic Appl. Sci. **17**, 66 (2015). <https://doi.org/10.1016/j.jaubas.2014.02.004>
9. A.M. Pourrahimi, D. Liu, V. Strom, M.S. Hedenqvist, R.T. Olsson, U.W. Gedde, J. Mater. Chem. A **3**, 17190 (2015). <https://doi.org/10.1039/c5ta03120f>
10. G.M. Ali, P. Chakrabarti, Appl. Phys. Lett. **97**, e031116 (2010). <https://doi.org/10.1063/1.3467204>
11. W. Khan, F. Khan, H.M.S. Ajmal, N.U. Huda, J.H. Kim, S.D. Kim, Nanomaterials **8**, 68 (2018). <https://doi.org/10.3390/nano8020068>
12. N.M. Al-Hada, E.B. Saion, A.H. Shaari, M.A. Kamarudin, M.H. Flaifel, S.H. Ahmad, S.A. Gene, PLoS One **9**, e103134 (2014). <https://doi.org/10.1371/journal.pone.0103134>
13. P.J. Lee, E. Saion, N.M. Al-Hada, N. Soltani, Metals **5**, 2383 (2015). <https://doi.org/10.3390/met5042383>
14. J. Wang, S. Zhang, J. You, H. Yan, Z. Li, X. Jing, M. Zhang, Bull. Mater. Sci. **31**, 597 (2008)
15. U. Manzoor, F.T. Zahra, S. Rafique, M.T. Moin, M. Mujahid, J. Nanomater. **2015**, e189058 (2015). <https://doi.org/10.1155/2015/189058>
16. A.K. Zak, W.H. Abd. M.E. Majid, R. Abrishami, Yousefi, X-ray analysis of ZnO nanoparticles by Williamson-Hall and size-strain plot methods. Solid State Sci. **13**, 251 (2011). <https://doi.org/10.1016/j.solidstatesciences.2010.11.024>
17. V.D. Mote, Y. Purushotham, B.N. Dole, J. Theor. Appl. Phys. **6**, 6 (2012). <https://doi.org/10.1186/2251-7235-6-6>
18. A. Dumbrava, D. Berger, G. Prodan, C. Matei, F. Moscalu, A. Diacon, ECS J. Solid State Sci. Technol. **6**, P870 (2017). <https://doi.org/10.1149/2.0311712jss>
19. M.R. Parra, F.Z. Haque, J. Mater. Res. Technol. **3**, 363 (2014). <https://doi.org/10.1016/j.jmrt.2014.07.001>
20. Z.N. Kayani, F. Saleemi, I. Batool, Appl. Phys. A **119**, 713 (2015). <https://doi.org/10.1007/s00339-015-9019-1>
21. S. Bai, J. Hu, D. Li, R. Luo, A. Chen, C.C. Liu, IEEE Sens. J. **12**, 1122 (2012). <https://doi.org/10.1109/JSEN.2011.2166152>
22. A. Dumbrava, D. Berger, G. Prodan, F. Moscalu, Chalcogenide Lett. **13**, 105 (2016)
23. A. Dumbrava, D. Berger, G. Prodan, F. Moscalu, A. Diacon, Mater. Chem. Phys. **173**, 70 (2016). <https://doi.org/10.1016/j.matchemphys.2016.01.040>
24. A. Dumbrava, G. Prodan, D. Berger, M. Bica, Powder Technol. **270**, 197 (2015). <https://doi.org/10.1016/j.powtec.2014.10.012>
25. M.E. Brown, *Handbook of Thermal Analysis and Calorimetry, vol. 1, Principles and Practice*, p. 172 (Elsevier, Amsterdam, 1998) (**206**, **262**)
26. J. Li, J. Sun, Acc. Chem. Res. **50**, 2737 (2017). <https://doi.org/10.1021/acs.accounts.7b00366>
27. A. Dumbrava, G. Prodan, A. Georgescu, F. Moscalu, Bull. Mater. Sci. **38**, 1 (2015). <https://doi.org/10.1007/s12034-014-0793-8>
28. D. Raoufi, J. Lumin. **134**, 213 (2013). <https://doi.org/10.1016/j.jlumin.2012.08.045>
29. Y.T. Prabhu, K.V. Rao, V.S.S. Kumar, B.S. Kumari, World J. Nano Sci. Eng. **4**, 21 (2014). <https://doi.org/10.4236/wjnse.2014.41004>
30. H. Borchert, E.V. Shevchenko, A. Robert, I. Mekis, A. Kornowski, G. Grubel, H. Weller, Langmuir **21**, 1931 (2005)

31. T.M.K. Thandavan, S.M.A. Gani, C.S. Wong, R.M. Nor, J. Non-destruct. Eval. **34**, 14 (2015). <https://doi.org/10.1007/s10921-015-0286-8>
32. J.I. Langford, J. Appl. Cryst. **6**, 190 (1973). <https://doi.org/10.1107/S0021889873008460>
33. http://database.iem.ac.ru/mincryst/s_carta.php?ZINCITE+5364. Accessed 28 May 2018
34. A.K. Zak, W.H.A. Majid, M.E. Abrishami, R. Yousefi, Solid State Sci. **13**, 251 (2011). <https://doi.org/10.1016/j.solidstasci.2010.11.024>
35. M.M. Mikhailov, V.V. Neshchimenko, C. Li, S. He, D. Yang, J. Mater. Res. **24**, 19 (2009). <https://doi.org/10.1557/JMR.2009.0033>
36. J. Iqbal, B. Wang, X. Liu, D. Yu, B. He, R. Yu, New J. Phys. **11**, 063009 (2009). <https://doi.org/10.1088/1367-2630/11/6/063009>
37. J. Tauc, R. Grigorovici, A. Vancu, Phys. Status Solidi B **15**, 627 (1966). <https://doi.org/10.1002/pssb.19660150224>
38. A. Dumbrava, D. Berger, G. Prodan, F. Moscalu, A. Diacon, Z. Phys. Chem. **232**, 61 (2018). <https://doi.org/10.1515/zpch-2017-0005>
39. A. Gupta, S.S. Pandey, M. Nayak, A. Maity, S.B. Majumder, S. Bhattacharya, RSC Adv. **4**, 7476 (2014). <https://doi.org/10.1039/C3RA45316B>
40. V. Srikant, D.R. Clarke, J. Appl. Phys. **83**, 5447 (1998). <https://doi.org/10.1063/1.367375>
41. L.I. Berger, *Semiconductor Materials* (CRC Press, Boca Raton, 1997)
42. X.W. Sun, H.S. Kwok, J. Appl. Phys. **86**, 408 (1999). <https://doi.org/10.1063/1.370744>
43. S. Kakarndee, S. Juabrum, S. Nanan, Mater. Lett. **164**, 198 (2016). <https://doi.org/10.1016/j.matlet.2015.10.154>
44. C. Bekeny, T. Voss, H. Gafsi, J. Gutowski, B. Postels, M. Kreye, A. Waag, J. Appl. Phys. **100**, 104317 (2006). <https://doi.org/10.1063/1.2390548>
45. T. Singh, T. Lehnen, T. Leuning, D. Sahu, S. Mathur, Appl. Surf. Sci. **289**, 27 (2014). <https://doi.org/10.1016/j.apsusc.2013.10.071>
46. M. Gerigk, P. Ehrenreich, M.R. Wagner, I. Wimmer, J.S. Reparaz, C.M.S. Torres, L. Schmidt-Mendea, S. Polarz, Nanoscale **7**, 16969 (2015)
47. B. Liu, X. Zhao, C. Terashima, A. Fujishima, K. Nakata, Phys. Chem. Chem. Phys. **16**, 8751 (2014). <https://doi.org/10.1039/c3cp55317e>
48. G.C. Park, T.Y. Seo, C.H. Park, J.H. Lim, J. Joo, Ind. Eng. Chem. Res. **56**, 8235 (2017). <https://doi.org/10.1021/acs.iecr.7b01920>
49. N. Kumaresan, K. Ramamurthi, R. Ramesh Babu, K. Sethuraman, S. Moorthy Babu, Appl. Surf. Sci. **418**, 138 (2017). <https://doi.org/10.1016/j.apsusc.2016.12.231>
50. R.M. Thankachan, N. Joy, J. Abraham, N. Kalarikkal, S. Thomas, O.S. Oluwafemi, Mater. Res. Bull. **85**, 131 (2017). <https://doi.org/10.1016/j.materresbull.2016.09.009>
51. N. Jain, A. Bhargava, J. Panwar, Chem. Eng. J. **243**, 549 (2014). <https://doi.org/10.1016/j.cej.2013.11.085>
52. A. Nageswara Rao, B. Sivasankar, V. Sadasivam, J. Hazard. Mater. **166**, 1357 (2009). <https://doi.org/10.1016/j.jhazmat.2008.12.051>
53. I.K. Konstantinou, T.A. Albanis, Appl. Catal. B Environ. **42**, 319 (2003)
54. H. Lachheb, E. Puzenat, A. Houas, M. Ksibi, E. Elaloui, C. Guillard, J.M. Herrmann, Appl. Catal. B Environ. **39**, 75 (2002). [https://doi.org/10.1016/S0926-3373\(02\)00078-4](https://doi.org/10.1016/S0926-3373(02)00078-4)